


**Topological states in a five-dimensional non-Hermitian system**Xingen Zheng<sup>1,\*,</sup> Tian Chen<sup>1,\*,†</sup> and Xiangdong Zhang<sup>1,‡</sup>*Key Laboratory of Advanced Optoelectronic Quantum Architecture and Measurements of Ministry of Education, Beijing Key Laboratory of Nanophotonics & Ultrafine Optoelectronic Systems, School of Physics, Beijing Institute of Technology, 100081 Beijing, China* (Received 15 August 2023; revised 3 January 2024; accepted 25 January 2024; published 14 February 2024)

Revealing new topological phases is of utmost importance in both Hermitian and non-Hermitian systems due to their potential applications. Generally, topological phases depend on the dimension of the system. Previous studies have shown that five-dimensional (5D) Hermitian systems exhibit certain phases that are not supported by their lower-dimensional counterparts. Here, we investigate the topological properties of 5D non-Hermitian systems and discover topological phases, such as Yang monospheres, Fermi cylinder surfaces, Fermi arcs connecting the two Yang monospheres, and the 5D skin effect. The topological invariants characterizing these phases can be described by both the second Chern number and a quantized Berry phase of the Yang monosphere. Additionally, we conduct experiments on the circuit platform to experimentally confirm the existence of these topological phases. Our findings also leverage the concept of higher-dimension non-Hermitian Weyl physics to control electrical signals in the engineered circuits.

DOI: [10.1103/PhysRevB.109.085307](https://doi.org/10.1103/PhysRevB.109.085307)**I. INTRODUCTION**

In the past few decades, significant efforts have been devoted to the exploration of topological phases in various systems [1–5]. Topological phases exhibit remarkable phenomena in modern physics. For example, one prominent feature of topological phases in Hermitian systems is the emergence of topologically protected edge states. These states are robust against local perturbations and play a crucial role in the topological functionality of the underlying system. It is worth noting that topological phases are dimension dependent. Recent theoretical investigations have shown that five-dimensional (5D) systems can host topological phases, such as Yang monopoles and two-dimensional (2D) Weyl surfaces, which are characterized by a nonzero second Chern number [6,7]. Experimental verification of these topological states has been conducted in photonic crystals utilizing synthetic dimensions and in circuit platforms employing artificial spatial dimensions [8,9]. However, these studies primarily focus on Hermitian systems.

On the other hand, there has been a growing interest in the study of non-Hermitian systems, described by non-Hermitian Hamiltonians, in recent years. This interest stems not only from the fact that many physical properties require the description by non-Hermitian Hamiltonians due to dissipation but also because non-Hermitian systems reveal rich physics beyond the Hermitian regime [10–20]. Non-Hermitian Hamiltonians can induce novel topological phases and unique phenomena, such as anomalous edge states, skin effects, unidirectional transmission or reflection, enhanced sensitivity,

and more [13–20]. So far as is known, these phenomena are predominantly observed in systems with dimensions lower than 4. Hence, it raises the question of whether novel topological phases exist in 5D non-Hermitian systems.

In this work, we investigate topological phases in 5D non-Hermitian systems with and without the skin effect. To accomplish this, we construct non-Hermitian systems by introducing different non-Hermitian terms to a 5D Hermitian system. In these non-Hermitian systems, we discover topological phases, including Yang monospheres that possess both a second Chern number and a quantized Berry phase, Fermi cylinder surfaces connecting two Yang monospheres in momentum space, four-dimensional (4D) boundary surface states, and the Fermi arc connecting the two Yang monospheres alongside the skin effect. A significant highlight of our work lies in the experimental verification of these topological phases within non-Hermitian systems. The experimental validation is achieved through the utilization of a circuit platform, wherein we construct circuits that effectively simulate these topological phases. By conducting experimental tests, we successfully verify the observed phenomena and validate the existence of these intriguing topological phases.

**II. DESIGN OF TWO 5D NON-HERMITIAN SYSTEMS**

To study the non-Hermitian phenomena in 5D, we consider lattice structures as shown in Fig. 1(a), in which the cells are marked by red dots. Each cell contains four sites (*A*, *B*, *C*, and *D*). The solid and dashed (orange, blue, brown, green, and pink) lines represent the connection couplings among cells along the *x*, *y*, *z*, *u*, and *v* directions, respectively. Here, even Fig. 1(a) shows only a structure containing  $2 \times 2 \times 2 \times 2 \times 2$  cells; by extending such connections, the 5D lattice structure containing any  $N_x \times N_y \times N_z \times N_u \times N_v$  cells can be obtained. The concrete coupling relationships

\*These authors contributed equally to this work.

†chentian@bit.edu.cn

‡Corresponding author: zhangxd@bit.edu.cn

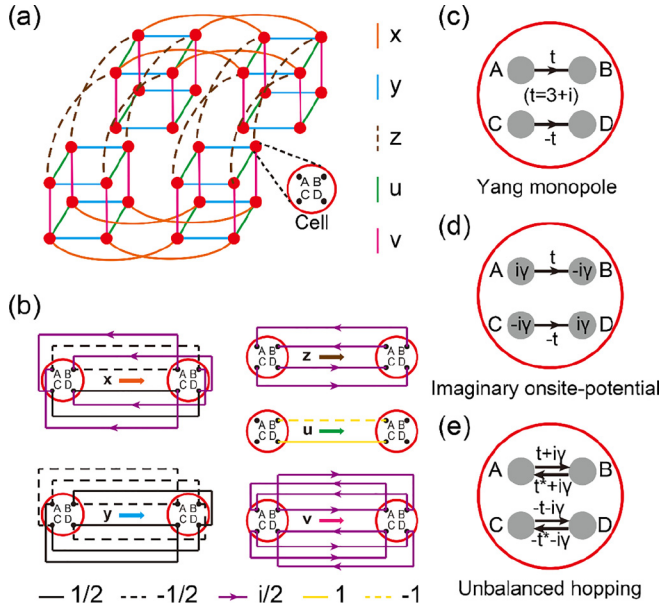


FIG. 1. (a) The scheme of coupling relationship between cells in the 5D lattice, in which the red dots represent the cells, and the orange, blue, brown, green, and pink lines represent the couplings in  $x$ ,  $y$ ,  $z$ ,  $u$ , and  $v$  directions, respectively. (b) The specific couplings between adjacent cells in each direction. The different kinds of lines represent different coupling strengths. (c), (d), and (e) are the specific intracell coupling and the onsite potential of the Yang monopole system, imaginary onsite-potential system, and unbalanced-hopping system, respectively.

and coupling strengths between sites in two adjacent cells along five directions are shown in Fig. 1(b), where the black solid, black dashed, purple arrowed, yellow solid, and yellow dashed lines represent the coupling strength of  $+1/2$ ,  $-1/2$ ,  $i/2$ ,  $1$ , and  $-1$ , respectively. Notice the arrow in the coupling strength of  $i/2$  denotes the electron-hopping direction, but if the electron hops from the opposite direction of the arrow, the coupling strength is  $-i/2$ . Besides the intercell coupling shown in Figs. 1(a) and 1(b), when proper intracell couplings and onsite potential are set, then both Hermitian or non-Hermitian 5D systems can be constructed. For example, when the intracell couplings  $t = 3 + i$  between sites A and B (C and D) are set as shown in Fig. 1(c), this 5D lattice represents the Hermitian Yang monopole system. Its Hamiltonian can be expressed as  $H_Y(\mathbf{k}) = \sum_{i=1}^5 \xi_i(\mathbf{k})\Gamma_i$ , where  $\Gamma_i$  are the five  $4 \times 4$  Gamma matrices satisfying the anticommutation relation. Here, we choose the representation  $\Gamma_{1,2,3,4,5} = \{\sigma_1, \sigma_2, \sigma_3\tau_1, \sigma_3\tau_2, \sigma_3\tau_3\}$ , where  $\sigma$  and  $\tau$  are both Pauli matrices. The functions  $\xi_i(\mathbf{k})$  are defined as  $\zeta_1 = \sin k_x$ ,  $\zeta_2 = \sin k_y$ ,  $\zeta_3 = \sin k_z + (3 - \cos k_x - \cos k_y - \cos k_u)$ ,  $\zeta_4 = \sin k_u + (1 - \cos k_v)$ , and  $\zeta_5 = \sin k_v$ , while Figs. 1(d) and 1(e) represent the two cases of 5D non-Hermitian systems. And, they can be constructed using the Yang monopole system by introducing a non-Hermitian term. In detail, when introducing staggered imaginary onsite potential to the Yang monopole system, which is equal to adding a non-Hermitian diagonal matrix  $i\gamma\Gamma_5$  ( $\gamma \in R$ ) to  $H_Y(\mathbf{k})$ , the 5D lattice becomes the non-Hermitian system as shown in Fig. 1(d). When introducing unbalanced intracell hopping to the Yang

monopole system, which is equal to adding a non-Hermitian matrix  $i\gamma\Gamma_3$  ( $\gamma \in R$ ) to  $H_Y(\mathbf{k})$ , the 5D lattice becomes the non-Hermitian system as shown in Fig. 1(e), so that the Hamiltonian of the two non-Hermitian systems can be expressed as

$$H(\mathbf{k}) = \sum_{i=1}^5 \xi_i(\mathbf{k})\Gamma_i + \begin{cases} i\gamma\Gamma_5 & \text{case 1} \\ i\gamma\Gamma_3 & \text{case 2} \end{cases}, \quad (1)$$

where case 1 and case 2 correspond to the non-Hermitian systems with imaginary onsite potential and unbalanced hopping, respectively. Obviously, when there is no non-Hermitian term, it comes back to the Yang monopole system, where there exist two fourfold degenerate points, or say Yang monopoles, in the momentum space, locating at  $\mathbf{k} = (0, 0, \pm\pi, 0, 0)$ . And, the Yang monopole can be regarded as the monopole with a  $U(2)$  field in the 5D space owning a second Chern number  $C_2 = \pm 1$ , which could be calculated by integrating the  $U(2)$  Berry curvature over the closing surfaces wrapping the Yang monopole [21]. These are parts of the basic characters of the Yang monopole system. However, the two cases of non-Hermitian systems given by Eq. (1) show some other remarkable characteristics. We introduce them in the following.

#### A. Case 1: The imaginary onsite-potential system

For case 1 in Eq. (1), the energy spectrum of Hamiltonian can be analytically obtained as  $\varepsilon = \pm\sqrt{\xi_1^2 + \xi_2^2 + \xi_3^2 + \xi_4^2 + (\xi_5 + i\gamma)^2}$ , having four bands totally but everywhere twofold degenerate. Then, the condition for the fourfold degenerate band crossing on the zero energy is

$$\xi_5 = 0 \\ \xi_1^2 + \xi_2^2 + \xi_3^2 + \xi_4^2 = \gamma^2. \quad (2)$$

This condition in Eq. (2) gives two constraints, so it gives the three-dimensional (3D) closed manifold in the 5D space. (Detailed proof for the topology in this case is given in Appendix A). In Fig. 2(a), we show a discrete changing process of the fourfold degenerate band crossing with  $\gamma$  from 0 to 1.1 in the 3D subspace of  $k_x$ ,  $k_z$ , and  $k_u$  with  $k_y = k_v = 0$ . All the shapes of band crossing corresponding to various  $\gamma$  are marked in Fig. 2(a). Obviously, when  $\gamma = 0$ , it goes back to the Yang monopole case as the two green dots shown in Fig. 2(a). But, when  $\gamma$  slowly increases to a small number ( $0 < \gamma < 1$ ), the two Yang monopoles became two fourfold degenerate 3D spheres with  $k_v = 0$  as shown in the figure. We name the sphere the Yang monosphere, which consists of exceptional points at which the eigenstates coalesce and the Hamiltonian becomes defective. Moreover, outside the sphere, the energy spectrum is pure real because the pseudo-Hermitian symmetry is satisfied, and vice versa. As  $\gamma$  increases, the two Yang monospheres become larger, and when  $\gamma > 1$ , the two spheres merge into one manifold and the topological phase transition occurs. Here in this paper, we only study the case when  $\gamma$  is a small number ( $0 < \gamma < 1$ ).

Remarkably, we find the second Chern number, which is used to depict the topological charge of the Yang monopole, still works for the Yang monosphere. As shown in Fig. 2(b),

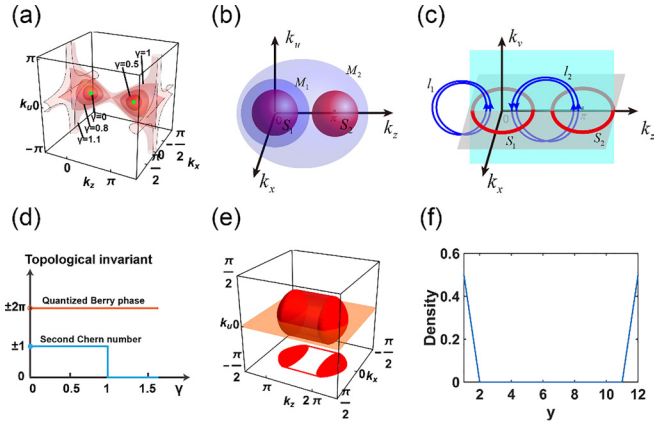


FIG. 2. (a) The band-crossing changing process with  $\gamma$  from 0 to 1.1. (b) The method of evaluating the second Chern number of the Yang monospheres. (c) The method of evaluating the quantized Berry phase of the Yang monospheres. (d) The two topological invariants of the second Chern number and quantized Berry phase with  $\gamma$ . (e) The Fermi cylinder surface and the solid Yang monopole in a 3D subspace of  $k_y = 0$  with an open boundary in the  $y$  direction. (f) The electron density distribution of the surface state along the  $y$  direction.

to obtain the second Chern number, we wrap one Yang monopole (the left red ball  $S_1$ ) by a 4D closed surface (the blue surface  $M_1$ ), on which the  $U(2)$  Berry curvature should be integrated. Specifically, the Berry connection is defined as  $A_i^{mn} = i\langle u_{\mathbf{k}}^m | \partial k_i | u_{\mathbf{k}}^n \rangle$ , where  $|u_{\mathbf{k}}^m\rangle$  ( $m = 1, 2$ ) denotes the two degenerate states of the valence bands. The  $U(2)$  Berry curvature can be expressed by  $F_{ij} = \partial k_i A_j - \partial k_j A_i - i[A_i, A_j]$ , with  $F_{ij} = -F_{ji}$ . Here, because the closing surface wrapping the Yang monopole satisfies the pseudo-Hermitian symmetry, we can still use only the right vector to calculate the second Chern number even though the non-Hermitian systems usually involve left vectors, so that the non-Abelian second Chern number of the Yang monopole can be evaluated by

$$C_2^{NA} = \oint_{S^4} \frac{d^4 k \epsilon^{ijkl} [\text{tr}(F_{ij} F_{kl}) - (\text{tr} F_{ij})(\text{tr} F_{kl})]}{32\pi^2}. \quad (3)$$

Notice the closed surfaces should be large enough to totally wrap the Yang monopole. And finally, the second Chern number of one Yang monopole can be obtained as  $\pm 1$ . That is to say, the topological charge of the Yang monopole still exists after it becomes a sphere, and that is the reason why we name it Yang monopole. Also, if the 4D closed surface wraps two Yang monopoles one time as shown by the larger blue surface  $M_2$  in Fig. 2(b), the result gives zero. This is because two Yang monopoles have different topological charges and they cancel out.

Besides the second Chern number, the topological invariant of such a Yang monopole can also be depicted by the manifold linking it. There is a rule that two closed manifolds of dimensions  $d_1$  and  $d_2$  can be nontrivially linked in a dimensional space with  $d_1 + d_2 + 1$ . For example, in 3D space, two one-dimensional (1D) circles can be linked together, forming a Hopf link. Therefore, in our 5D non-Hermitian system, we can use a 1D circle to link the 3D Yang monopole. Here, this topological invariant is called the quantized Berry phase, which is also used in Refs. [22,23]. In our case, it is evaluated

by integrating the Berry connection over the 1D trajectory linking the 3D sphere. This quantized Berry phase and the previous second Chern number are two different topological invariants that are both possessed by the Yang monopole. When linking the Yang monopole, because the 1D circle should go through the sphere, and inside the sphere the pseudo-Hermitian symmetry is broken, the energy eigenvalue is multivalued in the complex parameter space due to its square-root form. To solve this problem, the state should be defined over the Riemann surface, on which the state is single valued, but the closed trajectory should go through the sphere twice as the blue trajectories show in Fig. 2(c). Specifically, in our system, we separate the degenerate bands with a very small staggered potential energy first, then compute the quantized Berry phases of the two valence bands separately, and add them together to form the final quantized Berry phase. It is defined as

$$C_1 = \sum_{n=1,2} \left( \oint_{2l} i \langle \tilde{u}_{\mathbf{k}}^n | \partial_{\mathbf{k}} u_{\mathbf{k}}^n \rangle \cdot d\mathbf{k} \text{ mod } 4\pi \right), \quad (4)$$

where path  $2l$  travels across the Yang monopole twice over the Riemann surface, and  $\langle \tilde{u}_{\mathbf{k}}^n |$  and  $|u_{\mathbf{k}}^n\rangle$  are the  $n$ th normalized left and right eigenstates of the Hamiltonian, respectively. The final quantized Berry phase of one Yang monopole can be obtained as  $C_1 = \pm 2\pi$  (optionally mod  $4\pi$  for each band). Notice the 1D integrating trajectory is best to go through the Yang monopole along the  $k_y$  direction. That is because the Yang monopole exists in the 4D slice space with  $k_y = 0$ . The 1D trajectory like this links the Yang monopole successfully. The results also show that the sign of the quantized Berry phase is decided by the direction of the integrating trajectory. And, if you link two Yang monopoles at one time as shown by the  $l_2$  in Fig. 2(c), it gives zero. But, this zero result is different from the second Chern number, canceling out because of the opposite topological charge. This zero result is because, when linking two Yang monopoles at one time, the directions of the trajectory going through the two spheres are always opposite. If the trajectory  $l_2$  only links the right sphere  $S_2$ , it gives the same result as  $l_1$ . Actually, the quantized Berry phase comes from the exceptional point. The Yang monopole consists of exceptional points so that the quantized Berry phase exists. Moreover, even if the two Yang monopoles are merged together, this quantized Berry phase still exists. In Fig. 2(d), we show the change of these two topological invariants with  $\gamma$ . When  $\gamma > 1$ , the two monopoles merge together and the second Chern number becomes zero, while the quantized Berry phase comes from the exceptional point so that it still exists.

Another intriguing phenomenon of this non-Hermitian system is the Fermi cylinder surface. It is well known that in the Yang monopole lattice system, when an appropriate direction is opened, the Fermi arc connecting two Yang monopoles occurs, along with the boundary state, or say, surface state, on the 4D surface of the open direction [9]. However, in this non-Hermitian case with onsite gain and loss, we find significantly different situations. After we open the boundary along one direction (here we choose the  $y$  direction), what we observe is no longer a Fermi arc, but a hollow cylinder surface connecting the two Yang monopoles as shown in Fig. 2(e).

And, the two Yang monospheres become solid. In Fig. 2(e), we also draw the slice with  $k_u = 0$  (the orange plane) on the bottom part, showing the sphere is solid. This is somewhat similar to the case where, when opening a boundary, the nodal ring becomes the drumhead with a drumhead surface state in the 3D space [24]. Meanwhile, in this case, there exists a surface state on its 4D surface along the  $y$  direction under the open-boundary condition. In Fig. 2(f), we show the surface state through the electron density distribution along the  $y$  direction which corresponds to one zero-energy eigenvalue. The concentration of density distribution at the edge shows that this is indeed a surface state.

### B. Case 2: The unbalanced-hopping system

For case 2 in Eq. (1), the energy spectrum of Hamiltonian could be analytically obtained as  $\varepsilon = \pm\sqrt{\xi_1^2 + \xi_2^2 + (\xi_3 + i\gamma)^2 + \xi_4^2 + \xi_5^2}$ , having four bands totally but everywhere twofold degenerate. But this time, the condition for the fourfold band crossing on the zero energy ( $\varepsilon = 0$ ) becomes

$$\begin{aligned} \xi_3 &= 0 \\ \xi_1^2 + \xi_2^2 + \xi_4^2 + \xi_5^2 &= \gamma^2. \end{aligned} \quad (5)$$

This condition of Eq. (3) gives the 3D closed manifold in the 5D space. Actually, these two equations still give two 3D Yang monospheres when  $0 < \gamma < 1$ . Outside the sphere, the pseudo-Hermitian symmetry is satisfied and the energy is real. And, inside the Yang monosphere, the energy is imaginary. However, different from the imaginary onsite-potential system, neither of these two constraints have the condition like  $k_v = 0$  in the imaginary onsite-potential system which constrains the Yang monosphere in a certain slice subspace of 5D. Therefore, in this unbalanced-hopping non-Hermitian system, even if it is actually a 3D sphere in 5D space, it is distorted so much that we cannot totally observe the distorted spheres in a 3D slice subspace. Some lines of the Yang monosphere are only seen in the 3D subspace. This situation is like a twisted 1D circle in the 3D space; that is, the circle in the whole 3D space can be seen, but a complete circle cannot be seen in any 2D slice. Detailed proof for the topology of the 3D sphere in this case is given in Appendix A.

In Fig. 3(a), we show a discrete changing process of the fourfold degenerated crossing with  $\gamma$  from 0 to 1.2 in the 3D subspace of  $k_x$ ,  $k_z$ , and  $k_v$ , with  $k_y = k_u = 0$ . All values of  $\gamma$  are marked in it. Similar to the imaginary onsite-potential system of case 1, it gives two Yang monopoles. As  $\gamma$  increases from 0, the original Yang monopole expands into the Yang monosphere. When  $\gamma > 1$ , the two Yang monospheres merge into one. Here, we only study the Yang monosphere case ( $0 < \gamma < 1$ ). The Yang monosphere in this case also has two topological invariants: the second Chern number and the quantized Berry curvature. The calculation methods are the same. Only notice that when calculating the quantized Berry curvature, to link the Yang monosphere successfully, the 1D trajectory is best in the 2D plane formed by  $k_z$  and  $k_v$ . The results of the two topological invariants are also the same as those in case 1.

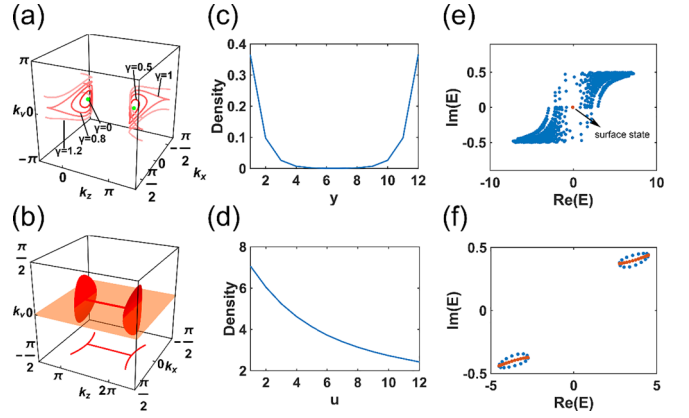


FIG. 3. (a) The changing process of band crossing with  $\gamma$  from 0 to 1.2 in the 3D subspace with  $k_y = k_u = 0$ . (b) The Fermi arc connected between two solid Yang monospheres in the subspace of  $k_u = 0$  with an open boundary along  $y$  direction when  $0 < \gamma < 1$ . (c) The electron density distribution showing the surface state in this system. During the calculation, the  $y$  direction is chosen as the open-boundary condition. (d) The electron density distribution showing the skin effect. In the calculation, the  $u$  direction is chosen as the open boundary condition. (e) The distribution of eigenvalues with only the  $y$  direction chosen open. The isolated zero-energy mode corresponding to the surface state is indicated as the orange dot. (f) The distribution of eigenvalues for the system with the  $y$  direction periodic (blue dots) and opened (red dots) in real space and other directions in momentum space.

When opening the boundary along an appropriate direction, here we choose the  $y$  direction; the Fermi object can be observed in the 3D subspace with  $k_u = 0$  as shown in Fig. 3(b). This shape of the Fermi object is totally different from the previous imaginary onsite-potential system in case 1. It is the Fermi arc (instead of the Fermi cylinder surface in case 1) connected between two 2D surfaces. Actually, these 2D surfaces in Fig. 3(b) are two Yang monospheres becoming solid after opening along the  $y$  direction, no longer some lines representing the Yang monosphere surfaces in Fig. 3(a). To show more clearly, we draw the slice with  $k_v = 0$  (the orange plane) on the bottom part.

Along with the Fermi object is the 4D surface state. As shown in Fig. 3(c), we calculated the electron density of the surface states with the open boundary in the  $y$  direction. From the distribution of the electron density, the phenomenon of electrons gathering at the edge apparently could be seen. These 4D surface states could be seen in the complex energy spectra as well. In Fig. 3(e), we show the distribution of eigenvalues with the open boundary in the  $y$  direction. The isolated zero-energy mode of the orange dot in the middle of the figure corresponds to the surface state.

Another remarkable phenomenon of this non-Hermitian system is the skin effect. We find there exists a strong skin effect along the  $u$  direction due to the unbalanced intracell hopping. As shown in Fig. 3(d), after opening the boundary along the  $u$  direction, we find that the electron density distribution along the  $u$  direction shows an apparent skin effect. We also calculated the decay length of the skin effect in the  $u$  direction. The decay length  $L$ , as an important quantity in the

skin effect, is defined as the length at which the electron density decays from the edge to  $1/e$  [25]. We refer to the method of solving the decay length in Refs. [25–27], and calculate the electron density distribution. Finally, we obtain the decay length  $L = \kappa^{-1}$ , where  $\kappa = \log(\sqrt{|(3+i+i\gamma)/(3-i+i\gamma)|})$  in the  $u$  direction for the unbalanced-hopping system.

The skin effect can also be verified from the distribution of eigenvalues. Here, in order to show the skin effect more clearly, we calculate the model in which the  $u$  direction is in real space and the other directions are in momentum space with  $(k_x, k_y, k_z, k_v) = (\pi/2, \pi/2, 0, \pi/2)$ , as shown in Fig. 3(f). The blue dots are the distribution of the eigenvalues with a periodic boundary condition in the  $u$  direction, while the orange dots are the distribution of the eigenvalues with an open boundary in the  $u$  direction. The blue dots surround the orange dots, which is also evidence of the skin effect [17,19,28]. In addition, the blue and orange dots in Fig. 3(f) are also related by decay length  $L$ , which can be obtained by solving the eigenvalues of the full momentum-space Hamiltonian  $H(\mathbf{k})$ . We choose  $(k_x, k_y, k_z, k_v) = (\pi/2, \pi/2, 0, \pi/2)$  and change the momentum in the  $u$  direction to get these blue dots. Then, following the method in Ref. [25], change  $k_u$  to  $k_u + i\kappa$ , where  $\kappa = L^{-1} = \log(\sqrt{|(3+i+i\gamma)/(3-i+i\gamma)|})$ . Finally, the orange dots can be obtained by solving the eigenvalue of the Hamiltonian  $H(k_u + i\kappa)$ , which is also the verification of the decay length.

### III. OBSERVATIONS OF TOPOLOGICAL PHASES AND SKIN EFFECT

A highlight of this work is the experimental verification of our two non-Hermitian systems based on the circuit platform. In the theory of simulating lattice systems by circuit, the circuit Laplacian plays the role of lattice Hamiltonian, and the positive and negative tunneling strengths between lattice sites are replaced by the inductor and capacitor. When simulating a non-Hermitian system, dissipation can be achieved with the resistor, while the gain can be achieved with an equivalent negative-resistor component which consists of two operational amplifiers and several resistors, as shown in the blue box of Fig. 4(c). The reason why this combination constitutes a negative resistor is given in Appendix B.

Previous works show that the circuit platform offers a key advantage to achieving high-dimension couplings: we only need to consider the connection relationship between different circuit nodes rather than their location [29–45]. The 5D circuit lattice could be built in a whole real space. However, since 5D lattice systems are usually very large, it is very difficult to build 5D lattice in the whole real space. For example, if there are four cells in each direction, the real-space Hamiltonian will be a huge matrix of  $4096 \times 4096$ . Our experiment chooses to use momentum space to simplify the construction of the circuit. It is easy to understand, for example, that the whole momentum-space Hamiltonian is a  $4 \times 4$  matrix, and it is easy to construct the experimental setup. Consider that the most prominent things are the Yang monosphere, the Fermi cylinder surface, and the Fermi arc in our two non-Hermitian systems, in which both two non-Hermitian systems have an open boundary in the  $y$  direction. Therefore, to observe these phenomena successfully and conveniently, we choose the

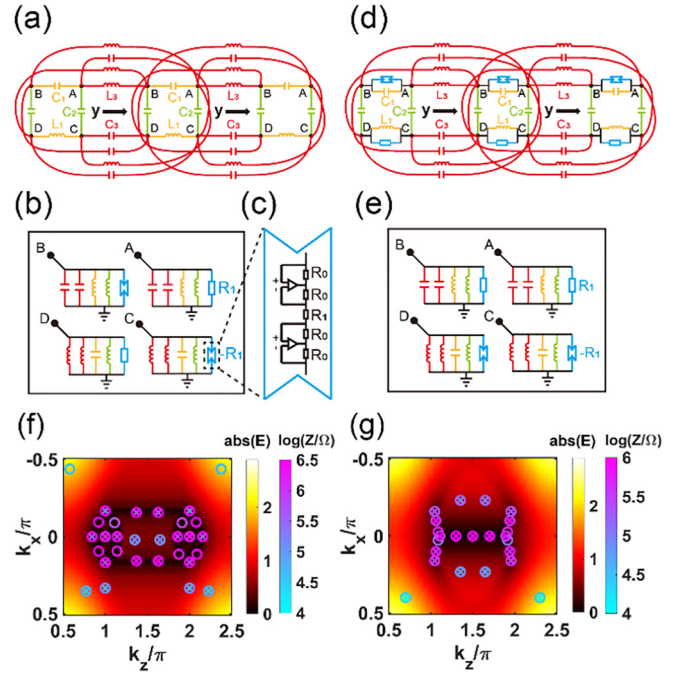


FIG. 4. (a) The circuit design of the imaginary onsite-potential system. (b) The grounding elements for a cell of the imaginary onsite-potential system. (c) The construction of the negative impedance module. (d) The circuit design of the unbalanced-hopping system. (e) The grounding elements for the unbalanced-hopping system. (f), (g) The experimental results of the imaginary onsite-potential system, respectively, in which the color map of hot represents the absolute value of the energy band closest to the Fermi surface, and the color map of cyan and pink represents the impedance of the circuit. The hollow circle and the cross represent the result of simulation and experiment, respectively.

$y$  direction in the real space and other directions in the momentum space to build up our experimental circuit setup.

Now, the master key becomes, how can we measure and get these Fermi objects in the circuit? We notice that these Fermi objects are all zero energies on the Fermi surface. And, in the circuit, the impedance  $Z_{ab}$  between two nodes  $a$  and  $b$  can be expressed as

$$Z_{ab} = \sum_n \frac{|\phi_n(a) - \phi_n(b)|^2}{j_n}, \quad (6)$$

where  $j_n$  is the  $n$ th eigenvalue of the circuit Laplacian  $J$ , and  $\phi_n(i)$  is the component of the  $n$ th eigenstate at node  $i$  ( $i = a, b$ ). In this case, the zero eigenvalue corresponds to a very small denominator in Eq. (6). Then, a large impedance appears. Therefore, the node impedance could be used to judge whether a dot in momentum space corresponds to a zero-energy eigenvalue. After judging many dots in the momentum space, these dots with high impedances in momentum space could form the shape of a Fermi cylinder surface, a Fermi arc, and the solid Yang monosphere. Here, in our experiment, a 2D slice of two non-Hermitian systems in momentum space is verified, respectively, by the circuit, which exactly corresponds to the 2D orange slice in Fig. 2(e) and Fig. 3(b).

For the imaginary onsite-potential system for case 1, the circuit design is shown in Fig. 4(a), where the circuit-connection relationship of three cells is depicted. Every cell has four sites:  $A$ ,  $B$ ,  $C$ , and  $D$ . Here, the circuit diagram in Fig. 4(a) only shows the connection of three cells, but the circuit of any  $N$  cells can be obtained by a simple extension. We define  $C0 = 0.5$  nF,  $L0 = 100$   $\mu$ H, and the resonant frequency  $f_0 = 1/\sqrt{L_0 C_0}$ . Then, we take  $C1 = C0[2 - \cos(kx) + \sin(kz)]$ ,  $L1 = L0/[2 - \cos(kx) + \sin(kz)]$ ,  $C2 = \sin(kx)C0$ ,  $L2 = L0/\sin(kx)$ ,  $C3 = 0.5 C0$  and  $L3 = L0/0.5$ ,  $R0 = 430 \Omega$  and  $R1 = 448 \Omega$ . In addition to the couplings between nodes, each node also needs suitable grounding elements to offset the degree matrix and set the onsite gain and loss. The grounding elements are shown in Fig. 4(b), where the resistor and negative-resistor module act, respectively, as onsite gain and loss. In this figure, only the grounding elements for the bulk nodes are shown, but the grounding elements for terminal nodes could be obtained by a few modifications based on the bulk nodes. We provide the detailed grounding elements for the terminal nodes in Appendix D. When the circuit is constructed as shown in Figs. 4(a), 4(b), and 3(c), it represents the imaginary onsite-potential non-Hermitian system with the real space of open boundary in the  $y$  direction and the momentum space in other directions. Similar to the imaginary onsite-potential system, the circuit design of the unbalanced-hopping system for case 2 is shown in Fig. 4(d), where the negative-resistor modules are added between sites  $A$  and  $B$ , and resistors between sites  $C$  and  $D$  in one cell. The resistors and negative-resistor modules represent the non-Hermitian coupling. The corresponding bulk grounding elements are shown in Fig. 4(e) and detailed grounding elements for the terminal nodes are provided in Appendix D. The detailed derivations of the circuit Laplacian about the two non-Hermitian systems are given in Appendix C. It is noticed that there will appear negative capacitors or negative inductors when  $k_x < 0$ . But actually, the negative capacitor is the inductor, and vice versa. Therefore, when  $k_x < 0$ , we only need to exchange  $C1$  and  $L1$ , as well as  $C2$  and  $L2$ . The circuit designs of the two systems when  $k_x < 0$  and other details are also given in Appendix D.

It is noticed that different positions in the momentum space (i.e., different  $\mathbf{k}$ ) correspond to the circuit components with different values. Therefore, to measure different points in the momentum space, there are two options. One method is to use the adjustable component. The capacitor and conductor can be adjusted to different values to realize different momentum points. The other method is to fabricate different circuits for every point. Considering the technical implementation, we take the second method, fabricating different circuits for every momentum point. It is also noticed that the circuit components in simulation can be set to any value, but in the real circuit, not all values have a corresponding component. The standard circuit components (capacitor, inductor, and resistor) only contain such values like 1, 3.3, 4.7, and so on. If we need a capacitor or inductor with other values, we should combine two or three different components in series or parallel to form the correct value. In Appendix E, we give the points measured in our real experiment, and how to use two or three components in series and parallel to form the corresponding value. The photos of our circuit

experimental setup and other details of constructing it are given in Appendix F.

In the experiment, we measured the impedance between nodes  $B$  and  $D$  of the first cell to determine whether the corresponding point in the momentum space is at zero energy. The results are shown in Figs. 4(f) and 4(g), which correspond to the imaginary onsite-potential system and unbalanced-hopping system, respectively. The color map of “hot” represents the absolute value of the energy band closest to the Fermi surface. The black region of zero-energy eigenvalues forms the shape of the Fermi object (Fermi cylinder surface and solid Yang monosphere), corresponding to the 2D orange plane of Figs. 2(e) and 3(b). The color map of “cyan and pink” represents the impedance of the circuit. Here, we use the hollow circle and the cross to represent the result of the simulation and experiment, respectively. It is clearly seen that the experimental results agree well with the simulated one. The impedances measured on the Fermi objects are higher, and the impedances measured elsewhere are lower. These high-impedance points form the Fermi cylinder surface, Fermi arc, and solid Yang monospheres.

The above two circuit experiments are both based on the 5D systems in which the  $y$  direction is in real space and the other four directions in momentum space with a fixed momentum value. The advantage of this experimental scheme is that it is convenient to observe the Fermi objects just by tracking the high-impedance (corresponds to the zero-admittance) positions in the momentum space. Our experimental results in Figs. 4(f) and 4(g) clearly show the topological structure as non-Hermitian Yang monosphere, Fermi cylinder surfaces, and Fermi arcs, which are totally different from those in the Hermitian cases. Moreover, in Appendix G, the 5D electric circuit in the full real space is constructed. With this circuit in real space, the electric simulation results of the distribution of voltages on the terminal nodes are provided, which demonstrates the skin effect.

#### IV. DISCUSSION AND CONCLUSION

In conclusion, we have constructed 5D non-Hermitian systems by introducing different non-Hermitian terms to the corresponding Hermitian systems. In these non-Hermitian systems, we have disclosed topological phases, including Yang monospheres that possess both a second Chern number and a quantized Berry phase, Fermi cylinder surfaces connecting two Yang monospheres in momentum space, 4D boundary surface states, and the Fermi arc connecting the two Yang monospheres alongside the skin effect. Furthermore, we have constructed the corresponding circuit platforms to demonstrate experimentally the existence of these topological states. Not only can the Yang monospheres be observed in the 5D non-Hermitian system, but we can also obtain the complex knot and link structures when we map the equation describing the band crossing to the equations describing the structures of the knots or links [46–49]. This we will leave for future work. Our work paves the way for employing topological circuit to study complex phenomena in 5D non-Hermitian systems. It also implies ways to control electrical signals and may have potential applications in the field of electronic signal control.

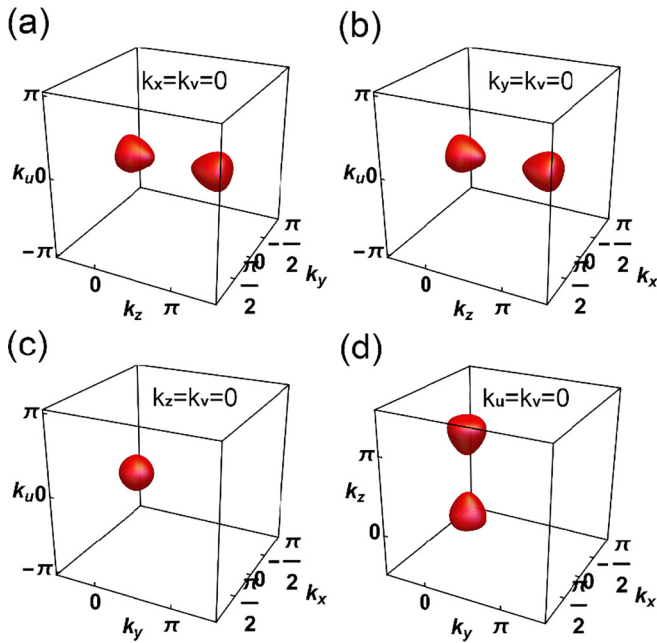


FIG. 5. Views of the 3D sphere surface in different 3D subspaces.

### ACKNOWLEDGMENTS

This work is supported by the National Key R&D Program of China under Grant No. 2022YFA1404900 and the National Natural Science Foundation of China (Grant No. 12234004).

### APPENDIX A: PROOF FOR THE TOPOLOGY OF 3D SPHERE SURFACE IN CASE 1 AND CASE 2

In case 1 of the main text, the manifold formed by the band crossing in the momentum space is described by the following equation:

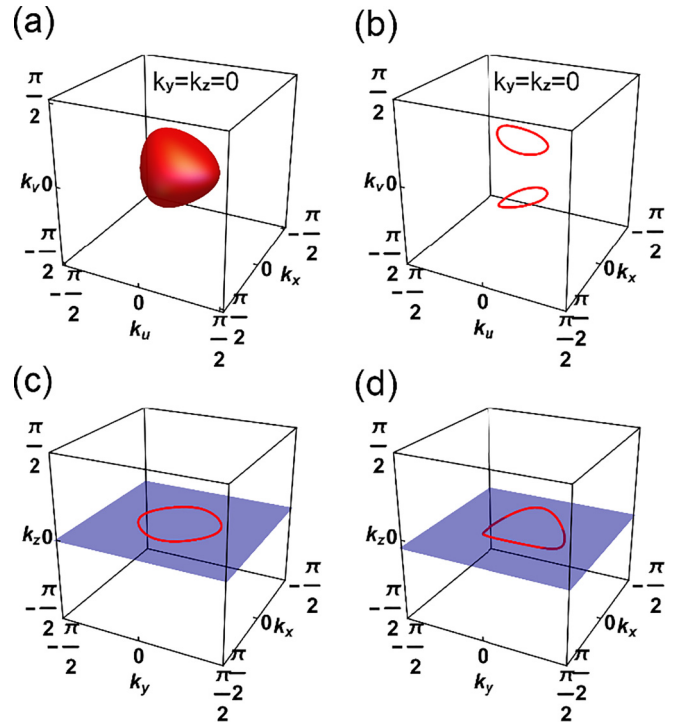
$$\begin{aligned} \xi_5 &= 0 \\ \xi_1^2 + \xi_2^2 + \xi_3^2 + \xi_4^2 &= \gamma^2, \end{aligned} \quad (\text{A1})$$

where the functions  $\xi_i(\mathbf{k})$  are defined as  $\zeta_1 = \sin k_x$ ,  $\zeta_2 = \sin k_y$ ,  $\zeta_3 = \sin k_z + (3 - \cos k_x - \cos k_y - \cos k_u)$ ,  $\zeta_4 = \sin k_u + (1 - \cos k_v)$ , and  $\zeta_5 = \sin k_v$ , and  $\gamma$  is a small real number. Obviously, this manifold exists in the 4D slice subspace with  $k_v = 0$ . Here, even if we do not have an eye on 5D or 4D, we could still judge the topology of this manifold by observing it in different 3D spaces. As shown in Figs. 5(a)–5(d), we find in all views of different 3D spaces that the manifolds are 2D sphere surfaces, so that we can know the topology of this manifold is the 3D sphere surface.

In case 2 of the main text, the manifold formed by the band crossing in the momentum space is described by the following equation:

$$\begin{aligned} \xi_3 &= 0 \\ \xi_1^2 + \xi_2^2 + \xi_4^2 + \xi_5^2 &= \gamma^2, \end{aligned} \quad (\text{A2})$$

where the functions  $\xi_i(\mathbf{k})$  are defined as  $\zeta_1 = \sin k_x$ ,  $\zeta_2 = \sin k_y$ ,  $\zeta_3 = \sin k_z + (3 - \cos k_x - \cos k_y - \cos k_u)$ ,  $\zeta_4 = \sin k_u + (1 - \cos k_v)$ , and  $\zeta_5 = \sin k_v$ . This equation also gives the 3D sphere surfaces. Here, we decide not to give strict


 FIG. 6. (a) The manifold in 3D subspace with  $k_z = 0$  before being pulled. (b) The manifold in 3D subspace with  $k_z = 0$  after being pulled. (c) The 1D circle in 3D space before being pulled. (d) The 1D circle in 3D space after being pulled.

mathematical proof because we are not mathematicians. But, being physicists, we decide to give a vivid explanation of why this equation represents the 3D sphere surface by analyzing the change of the manifold shape. At the beginning of this proof, let us consider another manifold first, which is described by

$$\begin{aligned} \xi_3 &= 0 \\ \xi_1^2 + \xi_2^2 + \xi_4^2 + \xi_5^2 &= \gamma^2 \end{aligned} \quad (\text{A3})$$

where the functions  $\xi_i(\mathbf{k})$  are defined as  $\zeta_1 = \sin k_x$ ,  $\zeta_2 = \sin k_y$ ,  $\zeta_3 = \sin k_z$ ,  $\zeta_4 = \sin k_u + (1 - \cos k_v)$ , and  $\zeta_5 = \sin k_v$ . The range of observation in the  $k$ -space is  $-\pi/2 < k_{x,y,u,v} < \pi/2$ . This manifold can be easily proved to be the 3D sphere surface, existing in the 4D slice subspace with  $k_z = 0$  (or  $k_z = \pi$ ). The proof method is the same as the previous case 1. We can observe the manifold in different 3D subspaces, and then obtain 2D sphere surfaces in all 3D subspaces, which indicates the manifold is the 3D sphere surface in the 5D. Here, we do not show all different 3D subspaces redundantly, but only give one of the 3D subspaces with  $k_y = k_z = 0$ , as shown in Fig. 6(a). We notice that from the view of the equation expression, this manifold and the previous manifold in case 2 only have some differences in the definition of  $\zeta_3$ , which actually means that the previous manifold in case 2 can be considered as a transformation from this manifold. In the condition of  $\xi_3 = 0$ , we think the values of  $k_x$ ,  $k_y$ , and  $k_u$  are not being additionally confined after the term  $(3 - \cos k_x - \cos k_y - \cos k_u)$  is added. However, to maintain the condition  $\xi_3 = 0$ ,  $k_z$  should vary correspondingly from the previous zero value. This variation of  $k_z$  can be understood

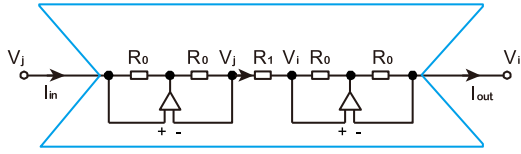


FIG. 7. The negative-resistor module.

as the previous manifold being pulled in the  $k_z$  direction so that the manifold can no longer totally exist in the 4D slice subspace with  $k_z = 0$ . And, if we still observe it in the 3D subspace with  $k_z = 0$ , only some parts of lines can be seen as shown in Fig. 6(b). The previous 2D sphere surface can no longer be totally observed. In this process of pulling, the topology of the manifold does not change, so it still belongs to the 3D sphere surface.

To describe this process more vividly, we also use a 1D circle to depict this process. At first, the 1D circle is described by

$$\begin{aligned} \xi_3 &= 0 \\ \xi_1^2 + \xi_2^2 &= \gamma^2 \end{aligned} \quad (\text{A4})$$

where  $\zeta_1 = \sin k_x$ ,  $\zeta_2 = \sin k_y$ , and  $\zeta_3 = \sin k_z$ . The range of observation in the  $k$ -space is  $-\pi/2 < k_{x,y,z} < \pi/2$ . We draw it in the 3D space, as shown in Fig. 6(c). Also, we can totally observe it in the 2D slice subspace with  $k_z = 0$ , corresponding to the blue slice in the figure. Then, we consider the case that  $\zeta_3$  changes to  $\zeta_3 = \sin k_z + (1 - \cos k_y)$ . As shown in Fig. 6(d), the 1D circle is pulled along the  $k_z$  direction. This time, we cannot observe it totally in the previous 2D slice, where only some dots belonging to the manifold exist. In this process of pulling, the topology of the manifold does not change, maintaining a 1D circle. This pulling process is similar to our 5D case; it does not change the topology of the manifold.

## APPENDIX B: ILLUSTRATION OF THE NEGATIVE-RESISTOR MODULE

In this section, we elucidate the mechanism by which our negative-resistor module functions as a negative resistor.

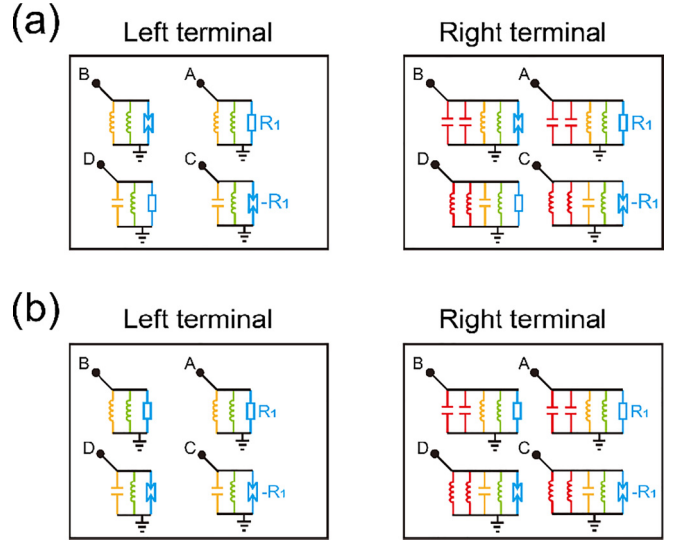


FIG. 8. (a), (b) The grounding elements of the imaginary onsite-potential system and unbalanced-hopping system, respectively.

The negative-resistor module consists of two operational amplifiers and several resistors. As depicted in Fig. 7, let us assume that the input voltage on the leftmost side is denoted as  $V_j$ , and the output voltage on the rightmost side is  $V_i$ . The amplifier operates under the condition known as a virtual short circuit, where its noninverting and inverting inputs maintain the same voltage, despite not being physically connected. Consequently, there are two additional nodes (located on either side of resistor  $R_1$ ) with voltages  $V_j$  and  $V_i$ , as indicated in the diagram. Assuming that the current flows towards the right, the current passing through  $R_1$  can be expressed as  $I(R_1) = (V_j - V_i)/R_1$ . We then utilize the second condition of the amplifier, known as a virtual open circuit, where no current flows through the branches connected to the noninverting and inverting inputs. By applying this condition, we can determine the current passing through all resistors with a value of  $R_0$ . Finally we get  $I_{in} = I_{out} = -I(R_1) = (V_j - V_i)/(-R_1)$ . Considering this module as a single component, it is equivalent to the resistor with a negative impedance.

## APPENDIX C: DERIVATION OF CIRCUIT LAPLACIAN IN THE MOMENTUM SPACE FOR THE TWO NON-HERMITIAN SYSTEM

For the imaginary onsite-potential system of case 1, the voltages on sites A, B, C, and D shown in Figs. 4(a) and 4(b) in the main text are represented by  $V_A$ ,  $V_B$ ,  $V_C$ , and  $V_D$ , respectively. The corresponding input currents are described by  $I_A$ ,  $I_B$ ,  $I_C$ , and  $I_D$ . The phase of the wave vector propagating along the y direction is denoted by  $k_y$ . After applying Kirchhoff's current law to the four nodes, we have

$$\begin{aligned} I_A &= i\omega C_1(V_A - V_B) + i\omega C_2(V_A - V_C) + \frac{1}{i\omega L_3}(V_A - V_B e^{ik_y}) + \frac{1}{i\omega L_3}(V_A - V_B e^{-ik_y}) + i\omega C_3(V_A - V_C e^{ik_y}) + \frac{1}{i\omega L_3}(V_A - V_C e^{-ik_y}) \\ &\quad + \frac{1}{i\omega L_1}(V_A - 0) + \frac{1}{i\omega L_2}(V_A - 0) + 2i\omega C_3(V_A - 0) + \frac{1}{R_1}(V_A - 0) \\ I_B &= i\omega C_1(V_B - V_A) + i\omega C_2(V_B - V_D) + \frac{1}{i\omega L_3}(V_B - V_A e^{ik_y}) + \frac{1}{i\omega L_3}(V_B - V_A e^{-ik_y}) + i\omega C_3(V_B - V_D e^{ik_y}) + \frac{1}{i\omega L_3}(V_B - V_D e^{-ik_y}) \\ &\quad + \frac{1}{i\omega L_1}(V_B - 0) + \frac{1}{i\omega L_2}(V_B - 0) + 2i\omega C_3(V_B - 0) + \frac{1}{-R_1}(V_B - 0) \end{aligned}$$



$$\begin{aligned}
 I_C &= \frac{1}{i\omega L_1}(V_C - V_D) + i\omega C_2(V_C - V_A) + \frac{1}{i\omega L_3}(V_C - V_A e^{ik_y}) + i\omega C_3(V_C - V_D e^{ik_y}) + i\omega C_3(V_C - V_A e^{-ik_y}) + i\omega C_3(V_C - V_D e^{-ik_y}) \\
 &\quad + \frac{1}{i\omega L_1}(V_C - 0) + i\omega C_2(V_C - 0) + \frac{2}{i\omega L_3}(V_C - 0) + \frac{1}{-R_1}(V_C - 0) \\
 I_D &= \frac{1}{i\omega L_1}(V_D - V_C) + i\omega C_2(V_D - V_B) + \frac{1}{i\omega L_3}(V_D - V_B e^{ik_y}) + i\omega C_3(V_D - V_C e^{ik_y}) + i\omega C_3(V_D - V_B e^{-ik_y}) + i\omega C_3(V_D - V_C e^{-ik_y}) \\
 &\quad + \frac{1}{i\omega L_1}(V_D - 0) + i\omega C_2(V_D - 0) + \frac{2}{i\omega L_3}(V_D - 0) + \frac{1}{R_1}(V_D - 0). \tag{C1}
 \end{aligned}$$

Equation (C1) can be written in the form of  $\mathbf{I} = \mathbf{J}\mathbf{V}$ . As the main text shows, we take  $C1 = C0[2 - \cos(kx) + \sin(kz)]$ ,  $L1 = [2 - \cos(kx) + \sin(kz)]/L0$ ,  $C2 = \sin(kx)C0$ ,  $L2 = \sin(kx)L0$ ,  $C3 = \gamma C0$ ,  $L3 = \gamma/L0$ , and  $R1 = \gamma\sqrt{L0/C0}\Omega$ . When the driving frequency is set as  $\omega = \omega_0 = 1/\sqrt{L0C0}$ , the circuit Laplacian  $\mathbf{J}$  in the momentum space can be simplified as

$$\mathbf{J} = i\sqrt{\frac{C_0}{L_0}} \begin{pmatrix} i\gamma & 1 - \cos k_x + \sin k_z & \sin k_x & 0 \\ 1 - \cos k_x + \sin k_z & -i\gamma & 0 & \sin k_x \\ \sin k_x & 0 & -i\gamma & -(1 - \cos k_x + \sin k_z) \\ 0 & \sin k_x & -(1 - \cos k_x + \sin k_z) & i\gamma \end{pmatrix}. \tag{C2}$$

When we neglect the unimportant coefficient  $i\sqrt{C_0/L_0}$  and set  $\Gamma_{1,2,3,4,5} = \{\sigma_1, \sigma_2, \sigma_3\tau_1, \sigma_3\tau_2, \sigma_3\tau_3\}$ , where  $\sigma$  and  $\tau$  are Pauli matrices, Eq. (C2) can be transformed to case 1 in Eq. (1) (the Hamiltonian of the imaginary onsite-potential system) in the main text in the 2D subspace with  $k_y = k_w = k_v = 0$ .

For the unbalanced-hopping system of case 2, the voltages on sites  $A$ ,  $B$ ,  $C$ , and  $D$  shown in Figs. 4(d) and 4(e) in the main text are represented by  $V_A$ ,  $V_B$ ,  $V_C$ , and  $V_D$ , respectively. The corresponding input currents are described by  $I_A$ ,  $I_B$ ,  $I_C$ , and  $I_D$ . The phase of the wave vector propagating along the  $y$  direction is denoted by  $k_y$ . After applying Kirchhoff's current law to the four nodes, we have

$$\begin{aligned}
 I_A &= i\omega C_1(V_A - V_B) + \frac{1}{-R}(V_A - V_B) + i\omega C_2(V_A - V_C) + \frac{1}{i\omega L_3}(V_A - V_B e^{ik_y}) + \frac{1}{i\omega L_3}(V_A - V_B e^{-ik_y}) + i\omega C_3(V_A - V_C e^{ik_y}) \\
 &\quad + \frac{1}{i\omega L_3}(V_A - V_C e^{-ik_y}) + \frac{1}{i\omega L_1}(V_A - 0) + \frac{1}{i\omega L_2}(V_A - 0) + 2i\omega C_3(V_A - 0) + \frac{1}{R_1}(V_A - 0), \\
 I_B &= i\omega C_1(V_B - V_A) + \frac{1}{-R}(V_B - V_A) + i\omega C_2(V_B - V_D) + \frac{1}{i\omega L_3}(V_B - V_A e^{ik_y}) + \frac{1}{i\omega L_3}(V_B - V_A e^{-ik_y}) + i\omega C_3(V_B - V_D e^{ik_y}) \\
 &\quad + \frac{1}{i\omega L_3}(V_B - V_D e^{-ik_y}) + \frac{1}{i\omega L_1}(V_B - 0) + \frac{1}{i\omega L_2}(V_B - 0) + 2i\omega C_3(V_B - 0) + \frac{1}{-R_1}(V_B - 0), \\
 I_C &= \frac{1}{i\omega L_1}(V_C - V_D) + \frac{1}{R}(V_C - V_D) + i\omega C_2(V_C - V_A) + \frac{1}{i\omega L_3}(V_C - V_A e^{ik_y}) + i\omega C_3(V_C - V_D e^{ik_y}) + i\omega C_3(V_C - V_A e^{-ik_y}) \\
 &\quad + i\omega C_3(V_C - V_D e^{-ik_y}) + \frac{1}{i\omega L_1}(V_C - 0) + i\omega C_2(V_C - 0) + \frac{2}{i\omega L_3}(V_C - 0) + \frac{1}{-R_1}(V_C - 0), \\
 I_D &= \frac{1}{i\omega L_1}(V_D - V_C) + \frac{1}{R}(V_D - V_C) + i\omega C_2(V_D - V_B) + \frac{1}{i\omega L_3}(V_D - V_B e^{ik_y}) + i\omega C_3(V_D - V_C e^{ik_y}) + i\omega C_3(V_D - V_B e^{-ik_y}) \\
 &\quad + i\omega C_3(V_D - V_C e^{-ik_y}) + \frac{1}{i\omega L_1}(V_D - 0) + i\omega C_2(V_D - 0) + \frac{2}{i\omega L_3}(V_D - 0) + \frac{1}{R_1}(V_D - 0). \tag{C3}
 \end{aligned}$$

Equation (C3) can be written in the form of  $\mathbf{I} = \mathbf{J}\mathbf{V}$ . Similar to the main text, we take  $C1 = C0[2 - \cos(k_x) + \sin(k_z)]$ ,  $L1 = [2 - \cos(k_x) + \sin(k_z)]/L0$ ,  $C2 = \sin(k_x)C0$ ,  $L2 = \sin(k_x)L0$ ,  $C3 = \gamma C0$ , and  $L3 = \gamma/L0$ , and  $R1 = \gamma\sqrt{L0/C0}\Omega$ . When the driving frequency is set as  $\omega = \omega_0 = 1/\sqrt{L0C0}$ , the circuit Laplacian  $\mathbf{J}$  in the momentum space can be simplified as

$$\mathbf{J} = i\sqrt{\frac{C_0}{L_0}} \begin{pmatrix} 0 & i\gamma + 1 - \cos k_x + \sin k_z & \sin k_x & 0 \\ i\gamma + 1 - \cos k_x + \sin k_z & 0 & 0 & \sin k_x \\ \sin k_x & 0 & 0 & -i\gamma - (1 - \cos k_x + \sin k_z) \\ 0 & \sin k_x & -i\gamma - (1 - \cos k_x + \sin k_z) & 0 \end{pmatrix}. \tag{C4}$$

When we neglect the unimportant coefficient  $i\sqrt{C_0/L_0}$  and set  $\Gamma_{1,2,3,4,5} = \{\sigma_1, \sigma_2, \sigma_3\tau_1, \sigma_3\tau_2, \sigma_3\tau_3\}$ , where  $\sigma$  and  $\tau$  are Pauli matrices, Eq. (C4) can be transformed to case 2 in Eq. (1) (the Hamiltonian of the unbalanced-hopping system) in the main text for the 2D subspace with  $k_y = k_w = k_v = 0$ .

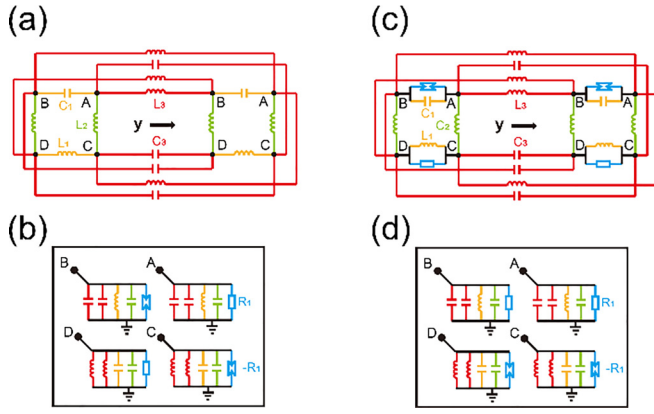


FIG. 9. (a), (b) The circuit design of the imaginary onsite-potential system when  $k_x < 0$ . (c), (d) The circuit design of the unbalanced-hopping system when  $k_x < 0$ . (a), (c) The connection relationship of the circuit between two adjacent plaquettes. (b), (d) The grounding elements.

#### APPENDIX D: THE CIRCUIT DESIGN SCHEME WHEN $k_x < 0$ AND OTHER DETAILS

The grounding mechanism we give in Figs. 4(b) and 4(e) is only for the bulk nodes. The grounding elements for terminal nodes could be obtained by a few modifications when compared with the bulk nodes. The following figures, Figs. 8(a) and 8(b), describe the grounding elements of the imaginary onsite-potential system and unbalanced-hopping system, respectively.

Our circuit design in Fig. 4 of the main text is specifically tailored for the case with  $k_x > 0$ . That is because, in our theory of simulating the tight-binding (lattice) model by circuit, the coupling strength in the lattice model corresponds to the admittance in the circuit, and we use the capacitor corresponding to the positive coupling strength and the inductor to negative. So, when  $k_x < 0$ , the circuit design shown in the main text can give the negative capacitor [ $C2 = \sin(k_x)C0$ ] and negative inductor [ $L2 = L0/\sin(k_x)$ ]. But actually, the negative capacitor corresponds to negative coupling strength; that is, the inductor. We call the capacitor and the inductor one pair when their admittances are opposite. When the driven frequency is the resonate frequency,  $C2$  and  $L2$  are one pair, as well as  $C1$

TABLE I. The coordinates of the points in the experiment and the combination of the standard components for the imaginary onsite-potential system.

$(kx/\pi, kz/\pi)$	$C1 = C0[2 - \cos(kx) + \sin(kz)]$	$L1 = L0/[2 - \cos(kx) + \sin(kz)]$	$C2 = C0 \sin(kx)$	$L2 = L0/\sin(kx)$
$(0.0199, 1.35) \& (0.0199, 1.65)$	110 pF  1 pF	330 $\mu$ H–120 $\mu$ H	62 pF  1 pF	470 $\mu$ H–330 $\mu$ H
$(0, 1) \& (0, 2)$	1 nF	100 $\mu$ H  100 $\mu$ H	Open circuit	Open circuit
$(0.15625, 1.6297) \& (0.15625, 1.3703)$	200 pF	150 $\mu$ H–100 $\mu$ H	470 pF	68 $\mu$ H–39 $\mu$ H
$(0, 1.1406) \& (0, 1.8594)$	510 pF  62 pF	39 $\mu$ H–47 $\mu$ H	Open circuit	Open circuit
$(0, 0.8437) \& (0, 2.1563)$	1 nF  470 pF	33 $\mu$ H–1 $\mu$ H	Open circuit	Open circuit
$(0.1667, 1) \& (0.1667, 2)$	1 nF  130 pF	39 $\mu$ H–4.7 $\mu$ H	1 nF–1 nF	100 $\mu$ H
$(0.3513, 0.7746) \& (0.3513, 2.2254)$	2.2 nF	22 $\mu$ H	910 pF  43 pF	56 $\mu$ H
$(0.3333, 2) \& (0.3333, 1)$	1.2 nF  300 pF	33 $\mu$ H–330 nH	820 pF  47 pF	56 $\mu$ H–1.8 $\mu$ H

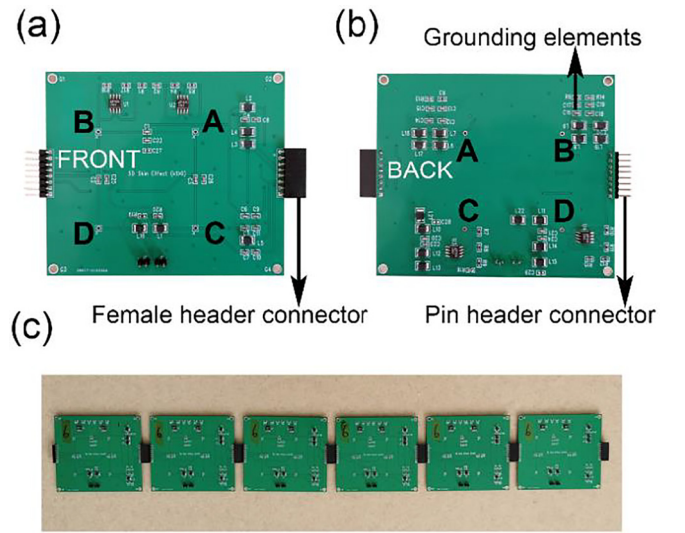


FIG. 10. (a), (b) The front and back views of the PCB module, respectively, corresponding to one cell in the lattice. (c) The whole experimental setup was formed by connecting the PCB modules.

and  $L1$ . Therefore, for the case of  $k_x < 0$ , we only need to exchange  $C2$  and  $L2$ . The concrete circuit design is shown in Fig. 9.

The derivation of this circuit Laplacian is also almost the same as the derivation when  $k_x > 0$  in the above Appendix A. The admittances of  $C2$  and  $L2$  only need to be exchanged, and we do not derive the circuit Laplacian repeatedly.

#### APPENDIX E: THE COORDINATES OF THE POINTS IN THE EXPERIMENT AND THE COMBINATION OF THE STANDARD COMPONENTS

The main text shows that we stipulate  $C0 = 0.5$  nF and  $L0 = 100$   $\mu$ H, then take  $C1 = C0[2 - \cos(kx) + \sin(kz)]$ ,  $L1 = L0/[2 - \cos(kx) + \sin(kz)]$ ,  $C2 = \sin(kx)C0$ ,  $L2 = L0/\sin(kx)$ ,  $C3 = 0.5C0$  and  $L3 = L0/0.5$ ,  $R0 = 430$   $\Omega$  and  $R1 = 448$   $\Omega$  in the circuit design. In the simulation, the circuit components can be set to any value, but in the real circuit not all values have a corresponding component. The standard circuit components (capacitor, inductor, and resistor) only

TABLE II. The coordinates of the points in the experiment and the combination of the standard components for the unbalanced-hopping system.

$(kx/\pi, kz/\pi)$	$C1 = C0[2 - \cos(kx) + \sin(kz)]$	$L1 = L0/[2 - \cos(kx) + \sin(kz)]$	$C2 = C0 \sin(kx)$	$L2 = L0/\sin(kx)$
(0, 1.7) & (0, 1.3)	100 pF  91 pF	180 $\mu$ H–82 $\mu$ H	Open circuit	Open circuit
(0, 1.893) & (0, 1.107)	560 pF  110 pF	68 $\mu$ H–6.8 $\mu$ H	Open circuit	Open circuit
(0.1, 1.94) & (0.1, 1.06)	820 pF  39 pF  2.4 pF	56 $\mu$ H–2.2 $\mu$ H	300 pF  9.1 pF	150 $\mu$ H–12 $\mu$ H
(0.16, 1.9533) & (0.16, 1.0467)	910 pF  62 pF  5.6 pF	39 $\mu$ H–12 $\mu$ H	470 pF  12 pF	100 $\mu$ H–3.9 $\mu$ H
(0.4, 2.3) & (0.4, 0.7)	2.4 nF  100 pF	10 $\mu$ H–10 $\mu$ H	910, pF  41 pF	47 $\mu$ H–5.6 $\mu$ H
(0.2323, 1.6474) & (0.2323, 1.3526)	360 pF	100 $\mu$ H–39 $\mu$ H	620, pF  47 pF	68 $\mu$ H–6.8 $\mu$ H
(0.2333, 1.8) & (0.2333, 1.2)	110 pF  560 pF	68 $\mu$ H–6.8 $\mu$ H	110 pF–560 pF	68 $\mu$ H–6.8 $\mu$ H

contain such values like 1, 3.3, 4.7, and so on. If we need the capacitor or inductor of other values, we should combine two or three different components in series or parallel to form the correct value.

For the imaginary onsite-potential system in Table I, we show the coordinates of the points chosen to experiment in the momentum space and how to get the correct value of the corresponding circuit components by combining two or three different components in series or parallel. To be concise, we use “||” to represent the components in parallel, and “—” to represent the components in series. And, because the capacitor and the inductor have different units of “F” and “H” in the table, the different units represent whether a component is a capacitor or inductor. If the capacitor is 0F or the inductor is infinite, it means there is no coupling between two nodes, which is equivalent to an open circuit. Here, Table I only shows the points when  $k_x > 0$ . For the case with  $k_x < 0$ , we choose the two points  $(-0.15625, 1.6297)$ , and  $(-0.1667, 1)$  to conduct the experiment. We just need to exchange the capacitor C2 and inductor L2 in the experiment of points  $(0.15625, 1.6297)$  and  $(0.1667, 1)$ .

For the unbalanced-hopping system, we show the corresponding details in Table II. All the agreements and operations are the same as those in Table I; only the coordinates of the points are different. For the case with  $k_x < 0$ , we choose the points  $(-0.1, 1.94)$ ,  $(-0.16, 1.9533)$ ,  $(-0.2323, 1.6474)$ , and  $(-0.2323, 1.8)$  to experiment.

#### APPENDIX F: THE PHOTOGRAPH OF THE EXPERIMENTAL SETUP AND OTHER DETAILS OF THE EXPERIMENT

Our experimental setup is shown in Fig. 10. Figures 10(a) and 10(b) are the front and back views of the PCB module, respectively, corresponding to one cell in the lattice. The front view of Fig. 10(a) contains the components of intracell and intracell coupling, while the back view of Fig. 10(b) contains the grounding components. We set the pin and female connectors on the edge of these printed circuit-board (PCB) modules so that the whole experimental setup can be formed by connecting these modules, as shown in Fig. 10(c).

We also use some simplifications in real experiments. When the negative-resistor module is grounded, it can be simplified as shown in Fig. 11, in which one of the two

operational amplifiers can be omitted after the simplification. This is the reason. The amplifier has the condition called a virtual short circuit in which its noninverting and inverting inputs have almost the same voltage even though they are not connected. As a result, under the action of the operation amplifier below, the voltage at node *b* is equal to the voltage at node *c* (the ground). This is equivalent to node *b* being directly grounded on the premise of the current at node *a* not being affected. Here, only the node *a* is a part of the non-Hermitian system and we only care that the current at the node *a* is not affected. Therefore, this negative-resistor module can be simplified as Fig. 11 shows when it is grounded. But, if neither end of this module is ground, one cannot simplify it. In the circuit design of the main text, we do not draw this simplification for a concise expression. But, we adopt this equivalent simplification for producing easily and saving money when creating the PCBs in the real experiment.

#### APPENDIX G: THE CIRCUIT SIMULATION RESULTS IN A FULLY REAL SPACE

In the main text, we have observed the location of the band crossing of two systems in the momentum space by tracking the high-impedance (corresponds to zero-admittance) positions. That is because we choose to establish the 5D system in which the *y* direction is in real space and the other four directions in momentum space with a fixed momentum value. Therefore, the high voltages at one of the terminal nodes for

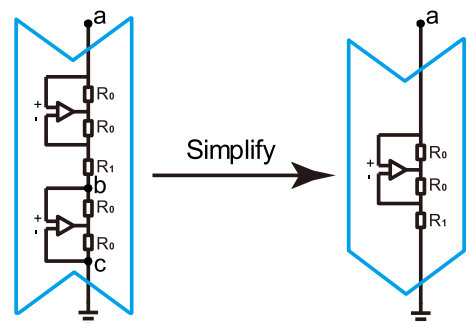


FIG. 11. The simplification when the negative-resistor module is grounded.

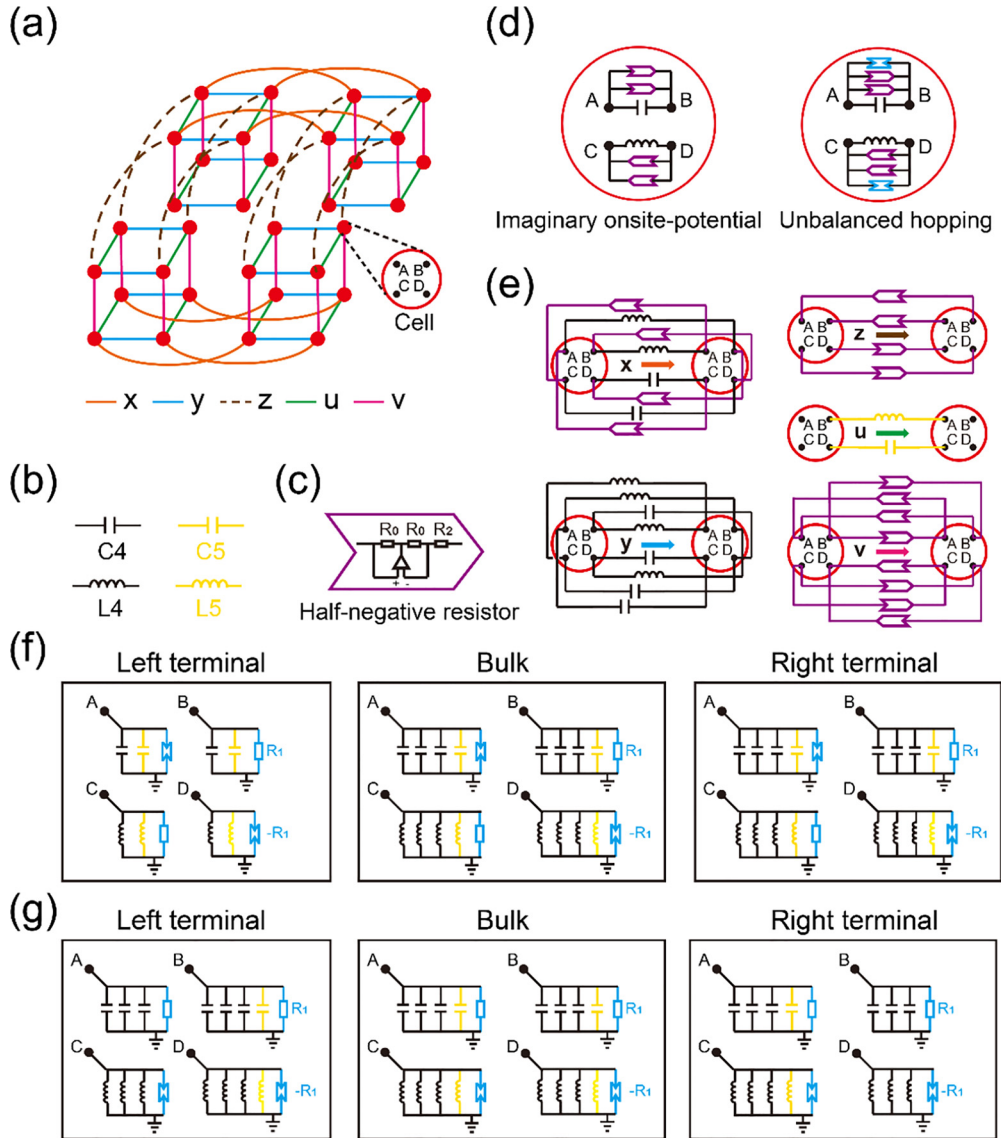


FIG. 12. (a) The scheme of connecting relationship between cells in the 5D circuit, in which the red dots represent the cells, and the orange, blue, brown, green, and pink lines represent the couplings in  $x$ ,  $y$ ,  $z$ ,  $u$ , and  $v$  directions, respectively. (b) The black–yellow capacitors and inductors are chosen as  $C4 = 0.25$  nF,  $C5 = 0.5$  nF,  $L4 = 200$   $\mu$ H, and  $L5 = 100$   $\mu$ H, respectively. (c) The scheme of the half-negative resistor module, which consists of one operational amplifier and three resistors. (d) The specific intracell connection between nodes and the onsite potential for the Yang monopole system and unbalanced-hopping system. (e) The specific connections between the nodes in adjacent cells in each direction. (f), (g) The grounding elements of left terminal nodes, bulk nodes, and right terminal nodes along the opened boundary for the imaginary onsite-potential and unbalanced-hopping system, respectively.

the 4D surface state or the skin effect cannot be observed in our circuit setup. Here, we give such a simulation through the circuit simulation software (LTSPICE) to show the surface state and the skin effect by node voltage measurements in full real space.

The circuit design for the 5D real space is shown in Fig. 12. The connecting relationship in the circuit and the lattice is the same. The difference is that the coupling strength in the lattice becomes the corresponding circuit component. The connecting relationship of two adjacent cells in five directions is shown in Fig. 12(a). Here, even Fig. 12(a) shows only a structure containing  $2 \times 2 \times 2 \times 2 \times 2$  cells; by extending such connections, the 5D lattice structure containing

any  $N_x \times N_y \times N_z \times N_u \times N_v$  cells can be obtained. As shown in Fig. 12(b), we choose the black–yellow capacitors and inductors  $C4 = 0.25$  nF,  $C5 = 0.5$  nF,  $L4 = 200$   $\mu$ H, and  $L5 = 100$   $\mu$ H, respectively. A half negative-resistor module was used, which contains one operational amplifier and three resistors, as shown in Fig. 12(c). The resistors are chosen to be  $R_0 = 430$   $\Omega$  and  $R_2 = 223.6$   $\Omega$ . This module is commonly used in Hermitian systems with imaginary number coupling, which could be seen as a normal resistor from left to right, but as a negative resistor from right to left [34]. The connecting relationships inside one cell for the two systems (imaginary onsite-potential and unbalanced-hopping systems) are shown in Fig. 12(d), where the blue negative-resistor module is

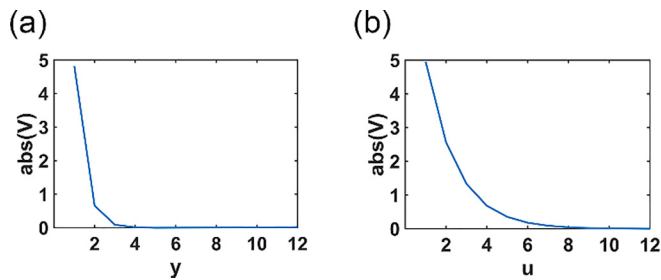


FIG. 13. (a) The voltage distribution along the  $y$  direction for the imaginary onsite-potential system. (b) The voltage distribution along the  $u$  direction for the unbalanced-hopping system.

totally the same as described in the previous experimental circuit design in Fig. 4(c). The concrete connecting relationships and circuit-component selection between sites in two adjacent cells along five directions for both the two systems are shown in Fig. 12(e), because they share the same intercell coupling. Here, we still only show the coupling of two adjacent cells, but a structure of any number of cells can be obtained simply by extending it with the same coupling.

When simulating the imaginary onsite-potential system in real space, we need to choose the open-boundary condition

along the  $y$  direction to observe the 4D surface state. In this situation, the grounding elements of the circuit are divided into three cases: left terminal nodes, bulk nodes, and right terminal nodes, shown in Fig. 12(f). When simulating the unbalanced-hopping system in real space, we need to choose the open-boundary condition along the  $u$  direction to observe the skin effect. In this situation, the grounding elements of the circuit are also divided into three cases, as shown in Fig. 12(g). By building the circuits this way, finally we obtain the two kinds of real-space five-dimensional circuits that we want to simulate.

In these two simulations, we stimulate node  $A$  of the first cell in the open-boundary direction by a stable sinusoidal signal voltage source, and then measure the voltage of node  $A$  of all other cells in that direction. The results are shown in Fig. 13. Figure 13(a) describes the voltages along the  $y$  direction in the imaginary onsite-potential system. Figure 13(b) describes the voltages along the  $u$  direction in the unbalanced-hopping system. From these voltage distributions, it is obvious that the two systems have the characteristics of surface state and skin effect, respectively: the surface state has only a very high voltage on the edge and the voltages on the rest of the nodes are almost zero, while the skin effect has an exponential decreased voltage distribution.

- [1] M. Z. Hasan and C. L. Kane, *Colloquium: Topological insulators*, *Rev. Mod. Phys.* **82**, 3045 (2010).
- [2] X.-L. Qi and S.-C. Zhang, *Topological insulators and superconductors*, *Rev. Mod. Phys.* **83**, 1057 (2011).
- [3] W. A. Benalcazar, B. A. Bernevig, and T. L. Hughes, *Quantized electric multipole insulators*, *Science* **357**, 61 (2017).
- [4] T. Ozawa, H. M. Price, A. Amo, N. Goldman, M. Hafezi, L. Lu, M. C. Rechtsman, D. Schuster, J. Simon, O. Zilberberg, and I. Carusotto, *Topological photonics*, *Rev. Mod. Phys.* **91**, 015006 (2019).
- [5] G. Ma, M. Xiao, and C. T. Chan, *Topological phases in acoustic and mechanical systems*, *Nat. Rev. Phys.* **1**, 281 (2019).
- [6] S. Sugawa, F. Salces-Carcoba, A. R. Perry, Y. Yue, and I. B. Spielman, *Second Chern number of a quantum-simulated non-Abelian Yang monopole*, *Science* **360**, 1429 (2018).
- [7] B. Lian and S.-C. Zhang, *Five-dimensional generalization of the topological Weyl semimetal*, *Phys. Rev. B* **94**, 041105(R) (2016).
- [8] S. Ma, Y. Bi, Q. Guo, B. Yang, O. You, J. Feng, H.-B. Sun, and S. Zhang, *Linked Weyl surfaces and Weyl arcs in photonic metamaterials*, *Science* **373**, 572 (2021).
- [9] X. Zheng, T. Chen, W. Zhang, H. Sun, and X. Zhang, *Exploring topological phase transition and Weyl physics in five dimensions with electric circuits*, *Phys. Rev. Res.* **4**, 033203 (2022).
- [10] D. Leykam, K. Y. Bliokh, C. Huang, Y. D. Chong, and F. Nori, *Edge modes, degeneracies, and topological numbers in non-Hermitian systems*, *Phys. Rev. Lett.* **118**, 040401 (2017).
- [11] S. Lieu, *Topological phases in the non-Hermitian Su-Schrieffer-Heeger model*, *Phys. Rev. B* **97**, 045106 (2018).
- [12] M.-A. Miri and A. Alù, *Exceptional points in optics and photonics*, *Science* **363**, eaar7709 (2019).
- [13] C. Poli, M. Bellec, U. Kuhl, F. Mortessagne, and H. Schomerus, *Selective enhancement of topologically induced interface states in a dielectric resonator chain*, *Nat. Commun.* **6**, 6710 (2015).
- [14] T. E. Lee, *Anomalous edge state in a non-Hermitian lattice*, *Phys. Rev. Lett.* **116**, 133903 (2016).
- [15] M. A. Bandres, S. Wittek, G. Harari, M. Parto, J. Ren, M. Segev, D. N. Christodoulides, and M. Khajavikhan, *Topological insulator laser: Experiments*, *Science* **359**, eaar4005 (2018).
- [16] G. Harari, M. A. Bandres, Y. Lumer, M. C. Rechtsman, Y. D. Chong, M. Khajavikhan, D. N. Christodoulides, and M. Segev, *Topological insulator laser: Theory*, *Science* **359**, eaar4003 (2018).
- [17] D. S. Borgnia, A. J. Kruchkov, and R.-J. Slager, *Non-Hermitian boundary modes and topology*, *Phys. Rev. Lett.* **124**, 056802 (2020).
- [18] L. Li, C. H. Lee, and J. Gong, *Topological switch for non-Hermitian skin effect in cold-atom systems with loss*, *Phys. Rev. Lett.* **124**, 250402 (2020).
- [19] N. Okuma, K. Kawabata, K. Shiozaki, and M. Sato, *Topological origin of non-Hermitian skin effects*, *Phys. Rev. Lett.* **124**, 086801 (2020).
- [20] W. Zhu and J. Gong, *Hybrid skin-topological modes without asymmetric couplings*, *Phys. Rev. B* **106**, 035425 (2022).
- [21] B. Lian and S.-C. Zhang, *Weyl semimetal and topological phase transition in five dimensions*, *Phys. Rev. B* **95**, 235106 (2017).
- [22] Y. Xu, S.-T. Wang, and L. M. Duan, *Weyl exceptional rings in a three-dimensional dissipative cold atomic gas*, *Phys. Rev. Lett.* **118**, 045701 (2017).
- [23] D.-W. Zhang, Y. Zhao, R.-B. Liu, Z.-Y. Xue, S.-L. Zhu, and Z. D. Wang, *Quantum simulation of exotic PT-invariant topological nodal loop bands with ultracold atoms in an optical lattice*, *Phys. Rev. A* **93**, 043617 (2016).
- [24] M. Biderang, A. Leonhardt, N. Raghuvanshi, A. P. Schnyder, and A. Akbari, *Drumhead surface states and their signatures in*

- quasiparticle scattering interference, *Phys. Rev. B* **98**, 075115 (2018).
- [25] C. H. Lee and R. Thomale, Anatomy of skin modes and topology in non-Hermitian systems, *Phys. Rev. B* **99**, 201103(R) (2019).
- [26] C. H. Lee, L. Li, and J. Gong, Hybrid higher-order skin-topological modes in nonreciprocal systems, *Phys. Rev. Lett.* **123**, 016805 (2019).
- [27] S. Yao and Z. Wang, Edge states and topological invariants of non-Hermitian systems, *Phys. Rev. Lett.* **121**, 086803 (2018).
- [28] K. Zhang, Z. Yang, and C. Fang, Correspondence between winding numbers and skin modes in non-Hermitian systems, *Phys. Rev. Lett.* **125**, 126402 (2020).
- [29] D. Zou, T. Chen, W. He, J. Bao, C. H. Lee, H. Sun, and X. Zhang, Observation of hybrid higher-order skin-topological effect in non-Hermitian topoelectrical circuits, *Nat. Commun.* **12**, 7201 (2021).
- [30] W. Deng, T. Chen, and X. Zhang,  $N$ th power root topological phases in Hermitian and non-Hermitian systems, *Phys. Rev. Res.* **4**, 033109 (2022).
- [31] J. Ningyuan, C. Owens, A. Sommer, D. Schuster, and J. Simon, Time- and site-resolved dynamics in a topological circuit, *Phys. Rev. X* **5**, 021031 (2015).
- [32] V. V. Albert, L. I. Glazman, and L. Jiang, Topological properties of linear circuit lattices, *Phys. Rev. Lett.* **114**, 173902 (2015).
- [33] S. Imhof *et al.*, Topoelectrical-circuit realization of topological corner modes, *Nat. Phys.* **14**, 925 (2018).
- [34] T. Hofmann, T. Helbig, C. H. Lee, M. Greiter, and R. Thomale, Chiral voltage propagation and calibration in a topoelectrical Chern circuit, *Phys. Rev. Lett.* **122**, 247702 (2019).
- [35] X.-X. Zhang and M. Franz, Non-Hermitian exceptional Landau quantization in electric circuits, *Phys. Rev. Lett.* **124**, 046401 (2020).
- [36] N. A. Olekhno *et al.*, Topological edge states of interacting photon pairs emulated in a topoelectrical circuit, *Nat. Commun.* **11**, 1436 (2020).
- [37] C. H. Lee *et al.*, Imaging nodal knots in momentum space through topoelectrical circuits, *Nat. Commun.* **11**, 4385 (2020).
- [38] T. Helbig *et al.*, Generalized bulk–boundary correspondence in non-Hermitian topoelectrical circuits, *Nat. Phys.* **16**, 747 (2020).
- [39] W. Zhang, D. Zou, Q. Pei, W. He, J. Bao, H. Sun, and X. Zhang, Experimental observation of higher-order topological Anderson insulators, *Phys. Rev. Lett.* **126**, 146802 (2021).
- [40] R. Li, B. Lv, H. Tao, J. Shi, Y. Chong, B. Zhang, and H. Chen, Ideal type-II Weyl points in topological circuits, *Natl. Sci. Rev.* **8**, nwa192 (2020).
- [41] M. Ezawa, Electric circuit simulations of  $n$ th-Chern-number insulators in  $2n$ -dimensional space and their non-Hermitian generalizations for arbitrary  $n$ , *Phys. Rev. B* **100**, 075423 (2019).
- [42] R. Yu, Y. X. Zhao, and A. P. Schnyder, 4D spinless topological insulator in a periodic electric circuit, *Natl. Sci. Rev.* **7**, 1288 (2020).
- [43] W. Zhang, D. Zou, J. Bao, W. He, Q. Pei, H. Sun, and X. Zhang, Topoelectrical-circuit realization of a four-dimensional hexadecapole insulator, *Phys. Rev. B* **102**, 100102(R) (2020).
- [44] Y. Wang, H. M. Price, B. Zhang, and Y. D. Chong, Circuit implementation of a four-dimensional topological insulator, *Nat. Commun.* **11**, 2356 (2020).
- [45] C. H. Lee, S. Imhof, C. Berger, F. Bayer, J. Brehm, L. W. Molenkamp, T. Kiessling, and R. Thomale, Topoelectrical circuits, *Commun. Phys.* **1**, 39 (2018).
- [46] J. Carlström, M. Stålhammar, J. C. Budich, and E. J. Bergholtz, Knotted non-Hermitian metals, *Phys. Rev. B* **99**, 161115(R) (2019).
- [47] L. Li, C. H. Lee, and J. Gong, Emergence and full 3D-imaging of nodal boundary Seifert surfaces in 4D topological matter, *Commun. Phys.* **2**, 135 (2019).
- [48] Z. Yang, C.-K. Chiu, C. Fang, and J. Hu, Jones polynomial and knot transitions in Hermitian and non-Hermitian topological semimetals, *Phys. Rev. Lett.* **124**, 186402 (2020).
- [49] K. Wang, A. Dutt, C. C. Wojcik, and S. Fan, Topological complex-energy braiding of non-Hermitian bands, *Nature (London)* **598**, 59 (2021).